

Majorana Zero Modes Induced by the Meissner Effect at Small Magnetic Field

Xiao-Hong Pan,^{1,2,3} Li Chen,⁴ Dong E. Liu,^{4,*} Fu-Chun Zhang,^{5,†} and Xin Liu^{1,2,3,‡}

¹School of Physics and Institute for Quantum Science and Engineering, Huazhong University of Science and Technology, Wuhan, Hubei 430074, China

²Hubei Key Laboratory of Gravitation and Quantum Physics and Wuhan National High Magnetic Field Center, Huazhong University of Science and Technology, Wuhan, Hubei 430074, China

³Wuhan Institute of Quantum Technology, Wuhan, Hubei 430074, China

⁴State Key Laboratory of Low Dimensional Quantum Physics, Department of Physics, Tsinghua University, Beijing, 100084, China

⁵Kavli Institute for Theoretical Sciences, University of Chinese Academy of Sciences, Beijing 100190, China



(Received 14 February 2023; accepted 28 November 2023; published 16 January 2024)

One key difficulty in realizing Majorana zero modes (MZMs) is the required high magnetic field, which causes serious issues, e.g., shrinks the superconducting gap, reduces topological region, and weakens their robustness against disorders. In this Letter, we propose that the Meissner effect can bring the topological superconducting phase to a superconductor/topological-insulator/superconductor (SC/TI/SC) hybrid system. Remarkably, the required magnetic field strength (< 10 mT) to support MZMs has been reduced by several orders of magnitude compared to that (> 0.5 T) in the previous schemes. Tuning the phase difference between the top and bottom superconductors can control the number and position of the MZMs. In addition, we account for the electrostatic potential in the superconductor/topological-insulator (SC/TI) interface through the self-consistent Schrödinger-Poisson calculation, which shows the experimental accessibility of our proposal. Our proposal only needs a small magnetic field of less than 10 mT and is robust against the chemical potential fluctuation, which makes the SC/TI/SC hybrid an ideal Majorana platform.

DOI: 10.1103/PhysRevLett.132.036602

Introduction.—Unpaired Majorana zero modes (MZMs) can only exist in systems with broken time-reversal symmetry, which usually requires applying a magnetic field. It is common in various strategies [1–28] to use the Zeeman splitting to cause the topological superconducting phase transition. The Zeeman splitting typically needs to be greater than the superconducting energy gap for this to occur. Therefore a magnetic field above a specific value is the prerequisite in various theoretical proposals and experimental detection. Meanwhile, a sizable and hard superconducting gap is necessary to isolate the MZMs from other low-energy states in the energy space to protect quantum information. However, a large magnetic field normally suppresses the *s*-wave superconducting gap. As a result, one of the most difficult challenges in implementing MZMs is to balance these two seemingly contradictory prerequisites. A recent experiment [29] observes the Meissner effect induced Doppler shift that can make the superconducting topological surface states have a segmented Fermi surface, a gapless superconducting state, under a small magnetic field about $B_c = 20$ mT. It thus suggests that a small magnetic field can significantly affect superconductivity [29], prompting us to wonder whether the Meissner effect can induce the topological superconducting phase transition at such a low magnetic field. In the recent studies, supercurrent has been proposed to induce

first-order topological phase transition [30,31]. Besides, a topological superconducting system with controllable number and position of MZMs is a prerequisite for implementing topological qubits. Higher-order topological superconductors [17–19,32–48] have shown their potential in fulfilling this condition [18,49–57].

In this Letter, we demonstrate that the Meissner effect can implement the second-order topological superconductivity and controllable Majorana zero modes in the superconductor/topological-insulator/superconductor (SC/TI/SC) sandwich junction [Fig. 1(a)] under a small magnetic field of less than 10 mT. An applied magnetic field parallel to the *x*-*y* plane induces the opposite diamagnetic current at the top and bottom SC/TI interfaces due to the Meissner effect [Fig. 1(b)]. Remarkably, this diamagnetic current causes the coexistence of two types of mass domain walls at the edge of the SC/TI/SC junction. The mass domain walls have multiple zeros where the unpaired MZMs are located [Fig. 1(b)] even if the applied magnetic field is less than 10 mT. Remarkably, the number and positions of MZMs can be controlled by the superconducting phase difference, as shown in the Supplemental Material [58], the applied magnetic field strength, and the system size. To be concrete, we perform a self-consistent Schrödinger-Poisson calculation to include the static potential at the SC/TI surface. The topological phase transition and MZMs

survive even when the surface Dirac point is far below the Fermi level due to the electrostatic potential and in the presence of disorders [58]. Last, we discuss the possible experimental implementation.

Continuous model.—We start with a continuous model of the SC/TI/SC junction without the magnetic field as [58,67]

$$H_0 = v(\hat{p}_x s_y - \hat{p}_y s_x) \rho_z \tau_z + [m + t(r)] \rho_x \tau_z - \mu \tau_z + \Delta \left[\frac{(1+\rho_z)}{2} \tau_x + \frac{(1-\rho_z)}{2} (\cos \phi \tau_x + \sin \phi \tau_y) \right], \quad (1)$$

with v and \hat{p} the TI surface state velocity and the momentum, respectively; μ the chemical potential; m and $t(r)$ the top-bottom layer hybridization through the bulk and lateral surfaces, respectively; Δ the superconducting gap amplitude; ϕ the superconducting phase difference; and the Pauli matrices ρ , τ , and s acting on the top-bottom surfaces, Nambu, and spin space, respectively. This model is valid when the TI thickness $l \ll d < \xi_{\text{TI}}$ with $l = \hbar v/M$ and $\xi_{\text{TI}} = \hbar v/\Delta$ the TI surface state decay length and coherence length respectively with M the TI bulk gap. For the NbSe₂/Bi₂Se₃ hybrid [7,68], $l \approx 1$ nm and $\xi_{\text{TI}} \approx 100$ nm cause $m \ll \Delta$. The open boundary condition (OBC) allows one to couple the top and bottom TI layers through the lateral surface, resulting in the radius r -dependent coupling coefficient $t(r)$ being finite at the boundary and negligibly small in the bulk [58]. Here, the system takes circular geometry for convenience. For $\phi = \pi$, the SC/TI/SC sandwich possesses helical Majorana edge modes protected by time-reversal symmetry [58,67]. When ϕ deviates from π as $\phi = \pi + \delta\phi$, it is equivalent to adding a uniform tunneling phase $\delta\phi/2$ in the interlayer coupling but keeping $\phi = \pi$ [58]. The interlayer coupling now takes [58]

$$H_J = t(r) \left[\cos\left(\frac{\delta\phi}{2}\right) \rho_x \tau_z - \sin\left(\frac{\delta\phi}{2}\right) \rho_y \tau_0 \right],$$

whose projection to the helical edge state subspace becomes

$$V_J = -\bar{t} \sin\left(\frac{\delta\phi}{2}\right) \tilde{s}_x = \bar{t} \cos\left(\frac{\phi}{2}\right) \tilde{s}_x, \quad (2)$$

with \tilde{s} the Pauli matrix acting on the helical edge state subspace and \bar{t} the expectation value of $t(r)$ on the edge states [58]. Note that Eq. (2) takes the exact form of the 4π -periodic Josephson effect with \bar{t} the Josephson coupling strength [69].

Now we apply a magnetic field B along the x axis. The Meissner effect causes the diamagnetic current parallel and antiparallel to the y axis at the top and bottom SC/TI interfaces, respectively [Fig. 1(b)]. As the magnetic field considered in this work is small (< 10 mT), the superconducting gap is still uniform due to the London rigidity [70,71]. Therefore, taking the London gauge [72,73], the

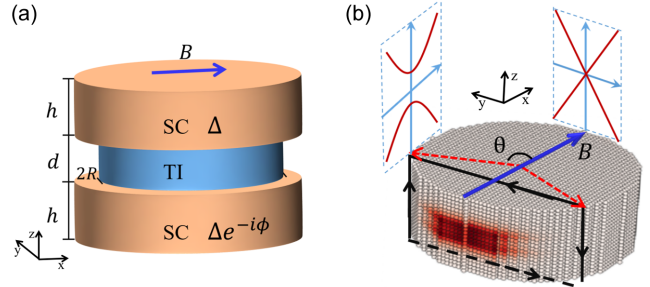


FIG. 1. (a) Schematic of the sandwich junction. (b) The density plot of MZMs at $B = 0.1B_c$, $\phi_{sc} = \pi$. B_c is the critical magnetic field strength to close the top-bottom surface superconducting gap due to the Doppler shift. The two spectrum plots schematically show the θ -dependent edge gap. The black and blue arrows indicate the vector potential under the London gauge and the magnetic field.

diamagnetic current affects the Hamiltonian of the system only through the vector potential. Firstly, the opposite diamagnetic currents lead to opposite vector potential at the top and bottom SC/TI interfaces [Fig. 1(b)] as $A = (0, B\lambda_L \rho_z, 0)$ [58] with λ_L the London penetration depth [29,74]. It modifies the momentum operator $\hat{p}_y \rightarrow \hat{p}_y + eA_y$ with $e > 0$ and gives an additional term

$$H_A = -evB\lambda_L \rho_0 s_x \tau_0, \quad (3)$$

which functions as an in-plane Zeeman effect and causes the Doppler shift at the top-bottom surfaces as [75,76]

$$E(k_x = 0) = s_x \rho_z evB\lambda_L \pm \sqrt{\Delta^2 + (\mu - s_x \rho_z \hbar v k_y)^2}. \quad (4)$$

The Doppler shift reduces [Fig. 2(a)] and eventually closes the system gap at $B_c = \Delta/(ev\lambda_L)$ [Fig. 2(b)], which remarkably is independent of the chemical potential as shown in Fig. 2(c). Therefore, in a wide range of chemical potential, we can take $B_c = \Delta/(ev\lambda_L)$ as the critical field to close the bulk superconducting gap. The diamagnetic current also affects the vector potential at the lateral surface: When taking OBC with the small magnetic field ($B < B_c$ [58]), the flux in the TI region [enclosed by the black rectangular in Fig. 1(b)] can be calculated as

$$B2dR \sin \theta = \oint \mathbf{A} d\mathbf{l} = 2[-B\lambda_L 2R \sin \theta + \delta\Phi(\theta)],$$

where the first and second terms in the above equation come from the vector potential at the top-bottom and lateral surfaces, respectively. Note that the first term contributes to the flux opposite to the total flux in this region [Fig. 1(b)], which gives $\delta\Phi(\theta) = B(2\lambda_L + d)R \sin \theta$ [58]. This also indicates a larger Doppler shift at the lateral surface and offers an additional θ -dependent phase $-\pi\delta\Phi(\theta)/\Phi_0 = -\eta \sin \theta$ into the electron tunneling from the bottom to the

top surfaces through the edge, with Φ_0 the magnetic quantum flux and

$$\eta = \frac{\pi BR(2\lambda_L + d)}{\Phi_0} = \frac{B}{B_c} \frac{R}{\xi_{\text{TI}}} \left(2 + \frac{d}{\lambda_L} \right) \quad (5)$$

a unitless parameter, characterizing the ratio between the flux through the SC/TI/SC junction and the magnetic quantum flux. The interlayer coupling through the lateral surface now becomes [58]

$$H_J = t(r) \left[\cos\left(\frac{\delta\phi}{2} - \eta \sin\theta\right) \rho_x \tau_z - \sin\left(\frac{\delta\phi}{2} - \eta \sin\theta\right) \rho_y \tau_0 \right].$$

Given the polar angle θ , we can project H_A of Eq. (3) into the edge state subspace and obtain the Jackiw-Rebbi Hamiltonian [58,77–79]

$$H_{\text{sf}}(\theta) = -i \frac{\hbar v_f}{R} \partial_\theta \tilde{s}_z + (V_A(\theta) + V_J(\theta)) \tilde{s}_x, \quad (6)$$

where

$$V_A(\theta) = -\Delta \frac{B}{B_c} \sin\theta, \quad V_J(\theta) = -\bar{t} \sin\left(\frac{\delta\phi}{2} - \eta \sin\theta\right) \quad (7)$$

correspond to H_A and H_J respectively [58]. The V_A is equivalent to the Zeeman splitting induced mass term in implementing two high-order Majorana corner states around $\theta = 0$ and π [16,18,22]. In a $\text{NbSe}_2/\text{Bi}_2\text{Te}_3$ hybrid, the magnetic field of 10 mT generates a gap of 0.25 meV, which implies the effective g -factor about 800 [29], much larger than all the g -factors in the current Majorana platform [11,80–83]. The V_J is a nested sine function and has multiple zeros at $\delta\phi/2 - \eta \sin\theta = n\pi$ with n an integer number and $\theta \in (0, 2\pi)$ [(Fig. 2(d)]. For $\eta < \pi$ and $\delta\phi = 0$, it has a similar potential to the first and together with the first term can produce two mass-sign changes as indicated by the black curves in Fig. 2(e). When increasing η by increasing either the magnetic field [green curve in Fig. 2(e)] or the system size (R or d) [brown curve in Fig. 2(e)] according to Eq. (6), there appear more mass-sign changes [Fig. 2(e)]. Note that each mass-sign change indicates the location of the unpaired MZM. When varying $\delta\phi$ and fixing $\eta = 1.2$ and $\eta = 3.6$, the location and number of MZMs are changed as shown by the black and brown curve in Fig. 2(e) for $\phi = \pi, 3\pi/4, \pi/2, \pi/4$, and 0. Therefore the second mass term has two advantages over the first one: We can control the MZM number by varying the magnetic field, the system size, or the superconducting phase difference; we can achieve unpaired MZMs in an even smaller magnetic field by increasing the system size.

Lattice model.—We now proceed to confirm the above analysis through the numerical simulation with Kwant [84] in the lattice model. Without applying a magnetic field, the lattice model for the SC/TI/SC sandwich takes the form

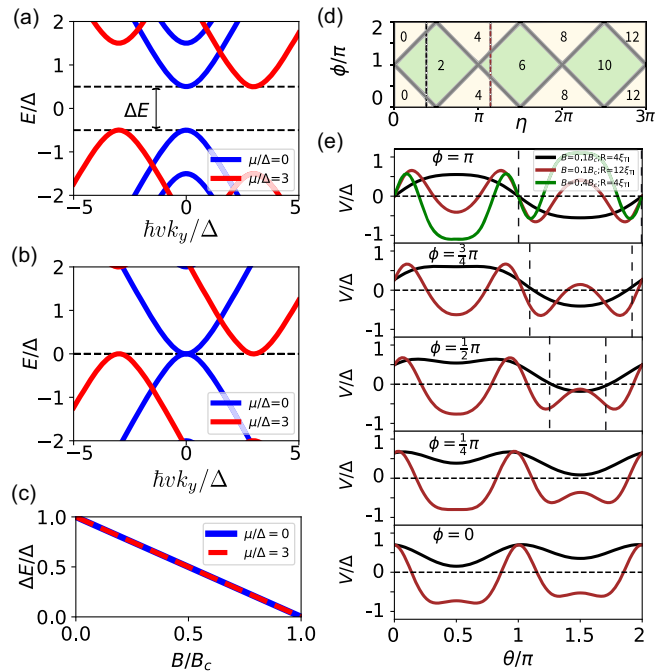


FIG. 2. In (a)–(c), the blue and red curves correspond to $\mu = 0$ and $\mu = 3\Delta$, respectively. (a),(b) Energy bands at $B = 0.5B_c$ and $B = B_c$; (c) Band gap as a function of B . (d) The number of the band gap zeros for $V_J(\theta)$ in the $\eta - \phi$ parameter space. (e) Given $d = \lambda_L$ and $\bar{t} = 0.7\Delta$, the magnitudes of the mass terms as the function of θ at $\phi = \pi, 3/4\pi, 1/2\pi, 1/4\pi, 0$ from top to bottom. With varying B and R , the black, red, and green curves correspond to $\eta = 1.2, 3.6, 4.8$, respectively.

$$H = \begin{bmatrix} H_{\text{TI}} + H_{\text{sc}} + H_c & \Delta(z) \\ \Delta^\dagger(z) & -s_y(H_{\text{TI}} + H_{\text{sc}} + H_c)^* s_y \end{bmatrix}, \quad (8)$$

with $\Delta(z) = \Delta$ for $z > d/2$, $\Delta(z) = \Delta e^{-i\phi}$ for $z < -d/2$, and $\Delta(z) = 0$ otherwise and d the thickness of TI [Fig. 1(b)]. The TI Hamiltonian H_{TI} in momentum space takes the form [85]

$$H_{\text{TI}} = \sum_i [M + 2t_i(1 - \cos k_i)] \sigma_z + \alpha_i \sin k_i \sigma_x \tilde{\sigma}_i - \mu,$$

with $i = x, y, z$, the Pauli matrices $\sigma, \tilde{\sigma}$ acting on the orbital and intrinsic angular momentum space, M, t_i, α_i the bulk gap, kinetic energy, and the spin-orbital coupling strength, respectively. The electronic Hamiltonian of the SC $H_{\text{sc}} = \hbar^2 k^2 / 2m_s - \mu_s$ with m_s and μ_s the effective mass and chemical potential respectively. The SC/TI coupling Hamiltonian takes $H_c = \sum_z -t_c c_{k,z+1}^\dagger c_{k,z} + h.c.$ with t_c the coupling strength. When applying the magnetic field, the vector potential under London gauge [86] generally takes

$$\begin{aligned} A_y(y, z) &= -f(y)g'(z) + 2B\lambda_L \frac{z}{d}, \\ A_z(y, z) &= f'(y)g(z). \end{aligned} \quad (9)$$

where $g(\pm d/2) = 0$ eliminates the z component of the vector potential at the SC/TI interface and $\oint \mathbf{A} \cdot d\mathbf{l} = BS_r$, the integration along the cross section edge and S_r the cross section area [Fig. 1(b)]. To satisfy these two conditions, we take $f(y) = \bar{B}y^2/2$, $g(z) = \text{sech}^2(z/z_0)$ with $d/z_0 \gg 1$ to satisfy the former and $\bar{B} = B(2\lambda_L + d)/2z_0$ to satisfy the latter.

Taking the periodic boundary condition (PBC) in the x direction, we calculate the edge state spectrum of the cross section corresponding to $\theta = \pm\pi/2$ [Fig. 1(b)]. At $\phi = \pi$, the junction has gapless edge states, indicated by the red dashed curves [Fig. 3(a)]. Applying the magnetic field along the x direction can gap the edge states [blue curves in Fig. 3(a)]. Then, for $(\phi, \eta) = (\pi, 0.5\pi)$, we numerically plot the edge gap magnitude (the absolute value of the minimal

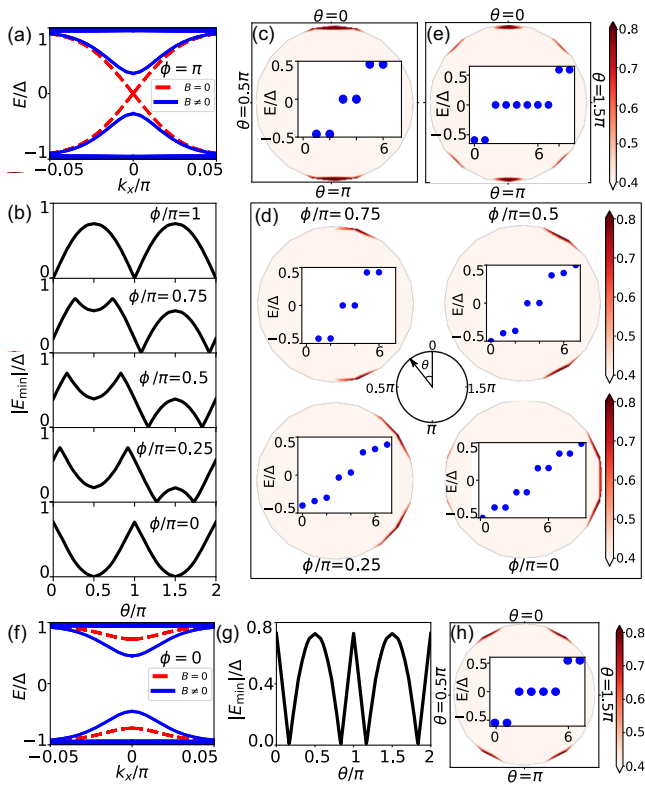


FIG. 3. Given d and R : (a),(f) The energy spectrum for $\theta = \pm\pi/2$ at $\phi = \pi$ and $\phi = 0$. The dashed red and solid blue curves correspond to $B = 0$ and $B \neq 0$. (b) The lowest positive eigenvalue as a function of θ for different ϕ at $\eta = 0.5\pi$. (c),(e),(h) The MZM density and several eigenvalues closest to the Fermi level at $(\phi, \eta) = (\pi, 0.5\pi)$, $(\pi, 1.5\pi)$, and $(0, \pi)$ respectively. Especially the calculation in (e) includes disorders. (d) Keeping $\eta = 0.5\pi$, the MZM density and several eigenvalues closest to the Fermi level for different ϕ . (g) The lowest positive eigenvalue as a function of θ at $(\phi, \eta) = (0, \pi)$. Parameters: $a = 1$ the lattice constant, $d = \lambda_L = 20$, $t_{x,y,z} = 1$, $M = -1.5$, $\alpha_{x,y,z} = 2$, $\mu = 0$, $\mu_{sc} = 1.75$, $t_c = 1$; in the SC region, $t_s = \hbar^2/2m_s = 1$ for hopping in the z direction and $t_s = 0$ for hopping in the x - or y direction; $R = 25$, $\Delta = 0.3$ in (c)–(e) and (h), and $R = 75$, $\Delta = 0.1$ in the others.

eigenenergy) as a function of θ . The edge states have only two gap zeros at $\theta = 0$ and $\theta = \pi$ [Fig. 3(b)] which is consistent with our continuous model analysis. We further show the number of MZMs and their distribution by taking OBC in all three directions in Fig. 3(c). Limited by the numerical resources, we remove the two SC layers and add superconducting pairing into the TI region within the $d/3$ thickness from the top and bottom surfaces while keeping other parameters unchanged in the MZM density calculation. The system exhibits two MZMs located around the gap zeros in Fig. 3(c), consistent with the analytical result in Fig. 2(d). To show the MZMs move, fixed at $\eta = 0.5\pi$ and different ϕ , we plot the gap magnitudes in Fig. 3(b) and the eigenenergies and the distributions of MZMs in Fig. 3(d), which demonstrate the consistent move of the gap zeros and the MZMs. When increasing η , more MZMs will appear. Fixed at $(\pi, 1.5\pi)$, the system generates six MZMS in Fig. 3(e). For $\phi = 0$, as shown by the red-blue curve in Fig. 3(f), the magnetic field can also affect the gap of the edge. This implies that gap zeros can occur even at $\phi = 0$. Thus, fixed at $(0, \pi)$, we plot the gap function in Fig. 3(g) and the distributions of MZMs in Fig. 3(h). The numerical results show that the system can generate four MZMs located around gap zeros. Our numerical results exhibit the perfect match with our analytical results in Figs. 2(d) and 2(e). These results confirm that the number of MZMs can be controlled by varying η and ϕ . Remarkably, our results are independent of the specific form of $f(y)$ and $g(z)$ [58].

Electrostatic potential.—In the practical scenario, the different work functions between SC and TI lead to the electrostatic field near the SC/TI interface and may deviate the Majorana physics from the ideal models [7,87,88]. Therefore we calculate the electrostatic potential $U(z)$ in TI using the Schrödinger-Poisson method [89–92]. The parameters of TI Hamiltonian and the relative dielectric constant $\epsilon_r = 25$ are the values of Bi_2Se_3 [58,85,93,94]. We only solve the Schrödinger equation in the TI region and treat the top-bottom SCs as the boundary condition $eU(z = \pm d/2) = W$ with W the band offset between the TI and SC [94,95]. The calculation neglects the magnetic field because it is small. The finite band offset W induces the electrostatic potential near the top and bottom TI surfaces [Fig. 4(a)]. We find that the TI spectrum is dramatically affected by the electrostatic potential: at $W = 0.35$ eV, the Dirac point is embedded deeply into the valence band, and more sub-bands other than the surface states appear at the Fermi energy [Fig. 4(b)]. Nevertheless, the electrostatic potential confines all the states at the Fermi surface within the 10 nm ($\ll \xi_{\text{TI}}$) range from the SC/TI interface, indicating good contact between the multibands in the TI and the SCs. To explore the proximity effect on these multibands, we calculate the bulk superconducting spectrum without a magnetic field by taking the PBC in x and y directions and show that all

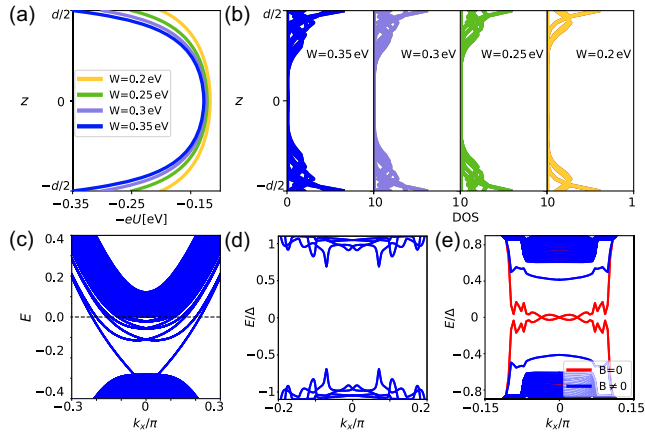


FIG. 4. (a),(b) The static potential $-eU(z)$ and electron density at the Fermi surface with different W . (c),(d) The electronic and superconducting band dispersion for $(k_x = 0, k_y)$ of the TI and SC/TI/SC junction, respectively, at $W = 0.35$ without a magnetic field. (e) Red and blue curves depict the superconducting band dispersion of the cross section for $\theta = \pm\pi/2$ in the $y-z$ plane of the SC/TI/SC junction with and without a magnetic field respectively. Parameters: $a = 1$ nm, $d = 30$ nm; $R = 1000$ nm; $M = -0.15$ eV; $\alpha_z = 0.22$ eV · nm; $\alpha_{x,y} = 0.44$ eV · nm; $t_z = 0.1$ eV · nm 2 ; $t_{x,y} = 0.566$ eV · nm 2 ; $\Delta = 1.5$ meV.

the states, at the Fermi surface possess a proximity gap greater than 0.7Δ [Fig. 4(d)]. Owing to this large proximity gap of the multibands, at $\phi = \pi$ and taking PBC only in the x direction, the SC/TI/SC sandwich shows clean gapless and gapped edge states without and with the magnetic field [Fig. 4(e)]. We further confirm numerically that the disorders only slightly reduce the topological gap, the energy of the first excited states, and do not affect the MZM existence [58]. These results indicate that our proposal remains valid in the presence of the electrostatic potential and disorders.

Discussion and conclusion.—Recently developed experimental techniques [96,97], such as top-down etching [98], can fabricate the SC/TI hybrid can grow superconductors to the side surfaces of TIs to fabricate SC/TI hybrids while keeping the TI bulk insulated. As our proposal has no requirement for the direction of the SC/TI/SC sandwich junction, this technique can be applied to our proposal, as shown in the Supplemental Material [58]. Therefore owing to the insulating bulk and finite thickness of TI, we can neglect the diamagnetic effect of the Josephson current [58,99]. In summary, we propose that the Meissner effect induced diamagnetic current can form MZMs in SC/TI/SC sandwich junctions when a small magnetic field (< 10 mT) is present. The diamagnetic current causes the Doppler shifts on TI surfaces, resulting in two sizable mass terms, which can implement MZMs with controllable numbers and positions. Further, incorporating the self-consistent Schrödinger-Poisson calculation, we show that our results are insensitive to the electrostatic potential near the SC/TI interface.

We acknowledge useful discussions with Tao Yu, Chao-Xing Liu, and Rui-Xing Zhang. X. L. acknowledges the support of the Innovation Program for Quantum Science and Technology (Grant No. 2021ZD0302700) and the National Natural Science Foundation of China (NSFC) (Grant No. 12074133). F.-C. Z. is partially supported by NSFC Grant No. 11674278, by the Chinese Academy of Sciences under Contract No. JZH KYPT-2021-08, and by the Priority Program of Chinese Academy of Sciences, Grant No. XDB28000000. D. E. L. is supported by the Innovation Program for Quantum Science and Technology (Grant No. 2021ZD0302400) and the National Natural Science Foundation of China (Grant No. 11974198). X.-H. P. is supported by China Postdoctoral Science Foundation (Grant No. 2023M731208).

*dongeliu@mail.tsinghua.edu.cn

[†]fuchun@ucas.ac.cn

[‡]phyliuxin@hust.edu.cn

- [1] J. D. Sau, R. M. Lutchyn, S. Tewari, and S. Das Sarma, *Phys. Rev. Lett.* **104**, 040502 (2010).
- [2] R. M. Lutchyn, J. D. Sau, and S. Das Sarma, *Phys. Rev. Lett.* **105**, 077001 (2010).
- [3] Y. Oreg, G. Refael, and F. von Oppen, *Phys. Rev. Lett.* **105**, 177002 (2010).
- [4] M. T. Deng, C. L. Yu, G. Y. Huang, M. Larsson, P. Caroff, and H. Q. Xu, *Nano Lett.* **12**, 6414 (2012).
- [5] L. P. Rokhinson, X. Liu, and J. K. Furdyna, *Nat. Phys.* **8**, 795 (2012).
- [6] A. Das, Y. Ronen, Y. Most, Y. Oreg, M. Heiblum, and H. Shtrikman, *Nat. Phys.* **8**, 887 (2012).
- [7] M.-X. Wang, C. Liu, J.-P. Xu, F. Yang, L. Miao, M.-Y. Yao, C. L. Gao, C. Shen, X. Ma, X. Chen, Z.-A. Xu, Y. Liu, S.-C. Zhang, D. Qian, J.-F. Jia, and Q.-K. Xue, *Science* **336**, 52 (2012).
- [8] H. O. H. Churchill, V. Fatemi, K. Grove-Rasmussen, M. T. Deng, P. Caroff, H. Q. Xu, and C. M. Marcus, *Phys. Rev. B* **87**, 241401(R) (2013).
- [9] W. Chang, S. M. Albrecht, T. S. Jespersen, F. Kuemmeth, P. Krogstrup, J. Nygård, and C. M. Marcus, *Nat. Nanotechnol.* **10**, 232 (2015).
- [10] H.-H. Sun, K.-W. Zhang, L.-H. Hu, C. Li, G.-Y. Wang, H.-Y. Ma, Z.-A. Xu, C.-L. Gao, D.-D. Guan, Y.-Y. Li, C. Liu, D. Qian, Y. Zhou, L. Fu, S.-C. Li, F.-C. Zhang, and J.-F. Jia, *Phys. Rev. Lett.* **116**, 257003 (2016).
- [11] S. M. Albrecht, A. P. Higginbotham, M. Madsen, F. Kuemmeth, T. S. Jespersen, J. Nygård, P. Krogstrup, and C. M. Marcus, *Nature (London)* **531**, 206 (2016).
- [12] J. Wiedenmann, E. Bocquillon, R. S. Deacon, S. Hartinger, O. Herrmann, T. M. Klapwijk, L. Maier, C. Ames, C. Brüne, C. Gould, A. Oiwa, K. Ishibashi, S. Tarucha, H. Buhmann, and L. W. Molenkamp, *Nat. Commun.* **7**, 10303 (2016).
- [13] S. Jeon, Y. Xie, J. Li, Z. Wang, B. A. Bernevig, and A. Yazdani, *Science* **358**, 772 (2017).
- [14] C.-X. Liu, J. D. Sau, and S. Das Sarma, *Phys. Rev. B* **95**, 054502 (2017).
- [15] H. Zhang *et al.*, *Nat. Commun.* **8**, 16025 (2017).

- [16] X. Zhu, *Phys. Rev. B* **97**, 205134 (2018).
- [17] T. Liu, J. J. He, and F. Nori, *Phys. Rev. B* **98**, 245413 (2018).
- [18] Y. Volpez, D. Loss, and J. Klinovaja, *Phys. Rev. Lett.* **122**, 126402 (2019).
- [19] X.-H. Pan, K.-J. Yang, L. Chen, G. Xu, C.-X. Liu, and X. Liu, *Phys. Rev. Lett.* **123**, 156801 (2019).
- [20] W. Liu, L. Cao, S. Zhu, L. Kong, G. Wang, M. Papaj, P. Zhang, Y.-B. Liu, H. Chen, G. Li, F. Yang, T. Kondo, S. Du, G.-H. Cao, S. Shin, L. Fu, Z. Yin, H.-J. Gao, and H. Ding, *Nat. Commun.* **11**, 5688 (2020).
- [21] L. Chen, B. Liu, G. Xu, and X. Liu, *Phys. Rev. Res.* **3**, 023166 (2021).
- [22] R.-X. Zhang and S. Das Sarma, *Phys. Rev. Lett.* **126**, 137001 (2021).
- [23] M. Papaj and L. Fu, *Nat. Commun.* **12**, 577 (2021).
- [24] Y.-M. Xie, K. T. Law, and P. A. Lee, *Phys. Rev. Res.* **3**, 043086 (2021).
- [25] R. Song, P. Zhang, and N. Hao, *Phys. Rev. Lett.* **128**, 016402 (2022).
- [26] M. Li, G. Li, L. Cao, X. Zhou, X. Wang, C. Jin, C.-K. Chiu, S. J. Pennycook, Z. Wang, and H.-J. Gao, *Nature (London)* **606**, 890 (2022).
- [27] D. Oshima, S. Ikegaya, A. P. Schnyder, and Y. Tanaka, *Phys. Rev. Res.* **4**, L022051 (2022).
- [28] X.-T. Chen, C.-H. Liu, D.-H. Xu, and C.-Z. Chen, *Chin. Phys. Lett.* **40**, 097403 (2023).
- [29] Z. Zhu, M. Papaj, X.-A. Nie, H.-K. Xu, Y.-S. Gu, X. Yang, D. Guan, S. Wang, Y. Li, C. Liu, J. Luo, Z.-A. Xu, H. Zheng, L. Fu, and J.-F. Jia, *Science* **374**, 1381 (2021).
- [30] A. Melo, S. Rubbert, and A. R. Akhmerov, *SciPost Phys.* **7**, 039 (2019).
- [31] K. Takasan, S. Sumita, and Y. Yanase, *Phys. Rev. B* **106**, 014508 (2022).
- [32] J. Langbehn, Y. Peng, L. Trifunovic, F. von Oppen, and P. W. Brouwer, *Phys. Rev. Lett.* **119**, 246401 (2017).
- [33] Z. Yan, F. Song, and Z. Wang, *Phys. Rev. Lett.* **121**, 096803 (2018).
- [34] Q. Wang, C.-C. Liu, Y.-M. Lu, and F. Zhang, *Phys. Rev. Lett.* **121**, 186801 (2018).
- [35] Y. Wang, M. Lin, and T. L. Hughes, *Phys. Rev. B* **98**, 165144 (2018).
- [36] C.-H. Hsu, P. Stano, J. Klinovaja, and D. Loss, *Phys. Rev. Lett.* **121**, 196801 (2018).
- [37] M. Ezawa, *Phys. Rev. B* **100**, 045407 (2019).
- [38] S. A. A. Ghorashi, X. Hu, T. L. Hughes, and E. Rossi, *Phys. Rev. B* **100**, 020509(R) (2019).
- [39] S. Franca, D. V. Efremov, and I. C. Fulga, *Phys. Rev. B* **100**, 075415 (2019).
- [40] R.-X. Zhang, W. S. Cole, X. Wu, and S. Das Sarma, *Phys. Rev. Lett.* **123**, 167001 (2019).
- [41] A. Tiwari, M.-H. Li, B. A. Bernevig, T. Neupert, and S. A. Parameswaran, *Phys. Rev. Lett.* **124**, 046801 (2020).
- [42] X. Wu, W. A. Benalcazar, Y. Li, R. Thomale, C.-X. Liu, and J. Hu, *Phys. Rev. X* **10**, 041014 (2020).
- [43] M. Kheirkhah, Z. Yan, Y. Nagai, and F. Marsiglio, *Phys. Rev. Lett.* **125**, 017001 (2020).
- [44] M. Kheirkhah, D. Zhu, J. Maciejko, and Z. Yan, *Phys. Rev. B* **106**, 085420 (2022).
- [45] Z. Wu and Y. Wang, *Phys. Rev. B* **106**, 214510 (2022).
- [46] M. Luo, *Phys. Rev. B* **106**, 235429 (2022).
- [47] D. Zhu, B.-X. Li, and Z. Yan, *Phys. Rev. B* **106**, 245418 (2022).
- [48] Y. Tan, Z.-H. Huang, and X.-J. Liu, *Phys. Rev. B* **105**, L041105 (2022).
- [49] Z. Yan, *Phys. Rev. B* **100**, 205406 (2019).
- [50] S.-B. Zhang, A. Calzona, and B. Trauzettel, *Phys. Rev. B* **102**, 100503(R) (2020).
- [51] S.-B. Zhang, W. B. Rui, A. Calzona, S.-J. Choi, A. P. Schnyder, and B. Trauzettel, *Phys. Rev. Res.* **2**, 043025 (2020).
- [52] T. E. Pahomi, M. Sigrist, and A. A. Soluyanov, *Phys. Rev. Res.* **2**, 032068(R) (2020).
- [53] M. F. Lapa, M. Cheng, and Y. Wang, *SciPost Phys.* **11**, 086 (2021).
- [54] L. Zhang and X.-J. Liu, *PRX Quantum* **3**, 040312 (2022).
- [55] M. Amundsen and V. Juricic, *Phys. Rev. Res.* **4**, 013088 (2022).
- [56] B. Lu and Y. Zhang, *J. Phys. Condens. Matter* **34**, 305302 (2022).
- [57] X. Wu, X. Liu, R. Thomale, and C.-X. Liu, *Natl. Sci. Rev.* **9**, nwab087 (2022).
- [58] See the Supplemental Material at <http://link.aps.org/supplemental/10.1103/PhysRevLett.132.036602> for the following: (1) The interlayer coupling Hamiltonian through the lateral surface; (2) The effective edge Hamiltonian of the BdG system; (3) The detail of vector potential distribution; (4) The numerical estimation of several critical fields; (5) Results independent on specific $f(y)$, $g(z)$ function; (6) The calculation of static potential; (7) The effect of chemical potential and disorder on Majorana zero modes; (8) The correlated length scales of the superconductor and topological insulator; (9) The details of numerical calculation; (10) The proposal to modulate the superconducting phase; (11) Meissner effect induced Majorana zero modes in a sandwiched junction with superconductors contacting the side surfaces of the topological insulator; (12) The Josephson current decays with increasing topological insulator thickness, which includes Refs. [59–66].
- [59] L. Fu and C. L. Kane, *Phys. Rev. B* **76**, 045302 (2007).
- [60] E.-W. Scheidt, M. Herzinger, A. Fischer, D. Schmitz, J. Reiners, F. Mayr, F. Loder, M. Baenitz, and W. Scherer, *J. Phys. Condens. Matter* **27**, 155701 (2015).
- [61] L. Zhang, J. Zhuang, Y. Xing, J. Li, J. Wang, and H. Guo, *Phys. Rev. B* **89**, 245107 (2014).
- [62] H. T. Lin, S. L. Wu, J. W. Wang, T. J. Chen, M. J. Wang, J. C. Chen, M. K. Wu, and C. C. Chi, *Supercond. Sci. Technol.* **28**, 085006 (2015).
- [63] R. F. Gasparovic and W. L. McLean, *Phys. Rev. B* **2**, 2519 (1970).
- [64] J. Bostock, K. Agyeman, M. H. Frommer, and M. L. A. MacVicar, *J. Appl. Phys.* **44**, 5567 (2003).
- [65] P. Townsend and J. Sutton, *Phys. Rev.* **128**, 591 (1962).
- [66] L. Bishop-Van Horn and K. A. Moler, *Comput. Phys. Commun.* **280**, 108464 (2022).
- [67] C.-X. Liu and B. Trauzettel, *Phys. Rev. B* **83**, 220510(R) (2011).
- [68] W. Dai, A. Richardella, R. Du, W. Zhao, X. Liu, C. X. Liu, S.-H. Huang, R. Sankar, F. Chou, N. Samarth, and Q. Li, *Sci. Rep.* **7**, 7631 (2017).
- [69] L. Fu and C. L. Kane, *Phys. Rev. Lett.* **100**, 096407 (2008).

- [70] F. London, *Phys. Rev.* **74**, 562 (1948).
- [71] J. Schrieffer, *Theory of Superconductivity* (CRC Press, Boca Raton, 1964).
- [72] F. London, H. London, and F. A. Lindemann, *Proc. R. Soc. A* **149**, 71 (1935).
- [73] J. Bardeen, *Phys. Rev.* **81**, 469 (1951).
- [74] J. D. Fletcher, A. Carrington, P. Diener, P. Rodière, J. P. Brison, R. Prozorov, T. Olheiser, and R. W. Giannetta, *Phys. Rev. Lett.* **98**, 057003 (2007).
- [75] R. W. Reinthalter, G. Tkachov, and E. M. Hankiewicz, *Phys. Rev. B* **92**, 161303(R) (2015).
- [76] N. F. Q. Yuan and L. Fu, *Phys. Rev. B* **97**, 115139 (2018).
- [77] R. Jackiw and C. Rebbi, *Phys. Rev. D* **13**, 3398 (1976).
- [78] B. A. Bernevig and T. L. Hughes, *Topological Insulators and Topological Superconductors* (Princeton University Press, Princeton, 2013).
- [79] Y. Wu, H. Liu, J. Liu, H. Jiang, and X. C. Xie, *Natl. Sci. Rev.* **7**, 572 (2019).
- [80] H. A. Nilsson, P. Caroff, C. Thelander, M. Larsson, J. B. Wagner, L.-E. Wernersson, L. Samuelson, and H. Q. Xu, *Nano Lett.* **9**, 3151 (2009).
- [81] T. D. Stanescu, R. M. Lutchyn, and S. Das Sarma, *Phys. Rev. B* **84**, 144522 (2011).
- [82] G. W. Winkler, D. Varjas, R. Skolasinski, A. A. Soluyanov, M. Troyer, and M. Wimmer, *Phys. Rev. Lett.* **119**, 037701 (2017).
- [83] A. Fornieri, A. M. Whiticar, F. Setiawan, E. Portolés, A. C. C. Drachmann, A. Keselman, S. Gronin, C. Thomas, T. Wang, R. Kallaher, G. C. Gardner, E. Berg, M. J. Manfra, A. Stern, C. M. Marcus, and F. Nichele, *Nature (London)* **569**, 89 (2019).
- [84] C. W. Groth, M. Wimmer, A. R. Akhmerov, and X. Waintal, *New J. Phys.* **16**, 063065 (2014).
- [85] H. Zhang, C.-X. Liu, X.-L. Qi, X. Dai, Z. Fang, and S.-C. Zhang, *Nat. Phys.* **5**, 438 (2009).
- [86] M. Tinkham, *Introduction to Superconductivity* (Courier Corporation, New York, 2004).
- [87] A. Kiejna and K. Wojciechowski, in *Metal Surface Electron Physics*, edited by A. Kiejna and K. Wojciechowski (Pergamon, Oxford, 1996), pp. 123–130.
- [88] J.-P. Xu, C. Liu, M.-X. Wang, J. Ge, Z.-L. Liu, X. Yang, Y. Chen, Y. Liu, Z.-A. Xu, C.-L. Gao, D. Qian, F.-C. Zhang, and J.-F. Jia, *Phys. Rev. Lett.* **112**, 217001 (2014).
- [89] I. Tan, G. L. Snider, L. D. Chang, and E. L. Hu, *J. Appl. Phys.* **68**, 4071 (1990).
- [90] J. H. Luscombe, A. M. Bouchard, and M. Luban, *Phys. Rev. B* **46**, 10262 (1992).
- [91] A. Ambrosetti, *Milan J. Math.* **76**, 257 (2008).
- [92] A. E. Antipov, A. Bargerbos, G. W. Winkler, B. Bauer, E. Rossi, and R. M. Lutchyn, *Phys. Rev. X* **8**, 031041 (2018).
- [93] M. Stordeur, K. K. Ketavong, A. Priemuth, H. Sobotta, and V. Riede, *Phys. Status Solidi (b)* **169**, 505 (1992).
- [94] L. Chen, Z. Cao, K. He, X. Liu, and D. E. Liu, *Phys. Rev. B* **107**, 165405 (2023).
- [95] A. E. G. Mikkelsen, P. Kotetes, P. Krogstrup, and K. Flensberg, *Phys. Rev. X* **8**, 031040 (2018).
- [96] Z. Zhang *et al.*, *Phys. Rev. Mater.* **7**, 086201 (2023).
- [97] T. Dvir, G. Wang, N. van Loo, C.-X. Liu, G. P. Mazur, A. Bordin, S. L. D. ten Haaf, J.-Y. Wang, D. van Driel, F. Zatelli, X. Li, F. K. Malinowski, S. Gazibegovic, G. Badawy, E. P. A. M. Bakkers, M. Wimmer, and L. P. Kouwenhoven, *Nature (London)* **614**, 445 (2023).
- [98] M. Rößler, D. Fan, F. Müning, H. F. Legg, A. Bliesener, G. Lippert, A. Uday, R. Yazdanpanah, J. Feng, A. Taskin, and Y. Ando, *Nano Lett.* **23**, 2846 (2023).
- [99] G.-W. Qiu and Y. Zhou, *Phys. Rev. B* **105**, L100506 (2022).